



Efficient photoinduced second-harmonic generation in silicon nitride photonics

Xiyuan Lu^{1,2}✉, Gregory Moille^{1,3}, Ashutosh Rao^{1,4}, Daron A. Westly¹ and Kartik Srinivasan^{1,3}✉

Silicon photonics lacks a second-order nonlinear optical ($\chi^{(2)}$) response in general, because the typical constituent materials are centrosymmetric and lack inversion symmetry, which prohibits $\chi^{(2)}$ nonlinear processes such as second-harmonic generation (SHG). Here, we realize high SHG efficiency in silicon photonics by combining a photoinduced effective $\chi^{(2)}$ nonlinearity with resonant enhancement and perfect phase matching. We show a conversion efficiency of $(2,500 \pm 100)\% \text{ W}^{-1}$ that is two to four orders of magnitude larger than previous field-induced SHG works. In particular, our devices realize milliwatt-level SHG output powers with up to $(22 \pm 1)\%$ power conversion efficiency. This demonstration is a breakthrough in realizing efficient $\chi^{(2)}$ processes in silicon photonics, and paves the way for further integration of self-referenced frequency combs and optical frequency references.

Second-order ($\chi^{(2)}$) nonlinear optics is a cornerstone for many classical and quantum applications¹. For example, to achieve compact functionalities for optical-frequency synthesis^{2,3} and optical atomic clocks⁴, frequency combs based on third-order ($\chi^{(3)}$) nonlinear processes need to be self-referenced by efficient second-harmonic generation (SHG), ideally on the same silicon chip. However, common materials in silicon photonics, including silicon (Si), silicon nitride (Si_3N_4) and silicon dioxide (SiO_2), do not support the $\chi^{(2)}$ response in bulk within the electric-dipole approximation¹. It is therefore particularly challenging to realize efficient SHG on a silicon chip (for example, for f - $2f$ locking in frequency combs⁵). As a result, systems based on silicon photonics technology have often relied on conventional platforms such as centimetre-scale periodically poled lithium niobate waveguides for $\chi^{(2)}$ functionalities^{2,4}. Alternatively, there has been considerable progress in realizing efficient SHG in non-silicon-based thin-film platforms, including aluminium nitride^{6–9}, gallium arsenide¹⁰ and lithium niobate^{11–15}. Such advances generally require heterogeneous integration with a silicon-based platform¹⁶ for optimized performance in the aforementioned frequency comb applications. On the other hand, silicon carbide nanophotonics has recently made major strides, demonstrating $\chi^{(2)}$ processes in both photonic-crystal cavities¹⁷ and microring resonators¹⁸. However, the fabrication processes that realize high performance in silicon carbide (SiC)^{17,18} suggest that its integration with the rest of the silicon photonics platform may be challenging.

There has also been work aiming to demonstrate effective $\chi^{(2)}$ processes directly in typical silicon photonics materials. One approach uses the weak $\chi^{(2)}$ nonlinearity present in silicon-based systems (for example, due to symmetry breaking) in conjunction with perfect phase matching in high-quality-factor (Q) microcavities to boost the normalized SHG efficiencies to $0.1\% \text{ W}^{-1}$ (ref. ¹⁹) and $0.049\% \text{ W}^{-1}$ (ref. ²⁰). These efficiencies can be improved by optimized input/output waveguide–resonator coupling, but are ultimately limited by the weakness of the $\chi^{(2)}$ nonlinearity. Another approach uses a large effective $\chi^{(2)}$ nonlinearity created through the

combination of an electric field and the medium's $\chi^{(3)}$ nonlinearity in photonic waveguides without cavity enhancement. This electric field can be induced directly by external electrodes²¹ or optically through the photogalvanic effect^{22–26}, and has resulted in $\chi^{(2)}$ nonlinearities up to 41 pm V^{-1} and normalized SHG efficiencies as high as $13\% \text{ W}^{-1}$ (ref. ²¹). The induced field not only produces a nonlinearity that substantially exceeds the existing intrinsic nonlinearity, but also supports quasi-phase matching (QPM), with phase either pre-determined²¹ or self-organized/photoinduced^{23,24,26}. However, the above approaches, when used separately, are inefficient compared to devices using traditional $\chi^{(2)}$ materials^{6,10,15} and, as a result, are far from generating milliwatt-level continuous-wave SHG output.

To realize efficient SHG, we engineered devices that take advantage of both a strong effective $\chi^{(2)}$ nonlinearity and resonant enhancement. We use the Si_3N_4 platform²⁷, which has been successfully applied to many wide-band nonlinear photonics demonstrations, including octave-spanning frequency combs^{28–30}, classical/quantum frequency conversion^{31,32} and optical parametric oscillation³³. Here, the physical process in use is photogalvanic field-induced SHG, first discovered in germanium-doped glass fibres decades ago³⁴. In contrast to reports of a photoinduced $\chi^{(2)}$ in non-resonant geometries such as Si_3N_4 waveguides^{22–26} and SiO_2 fibres^{34–38}, we demonstrate an effective photoinduced $\chi^{(2)}$ nonlinearity in a high- Q Si_3N_4 microresonator. We show that this resonantly enhanced, photoinduced $\chi^{(2)}$ nonlinear process enables high-efficiency SHG with appreciable output power for continuous-wave inputs.

The physical process behind our approach involves three $\chi^{(2)}$ and $\chi^{(3)}$ nonlinear interactions among three modes. The modes are illustrated in Fig. 1a, and consist of a direct-current (d.c.) mode, a pump mode and a second harmonic mode. The three interactions are illustrated in Fig. 1b, labelled I–III:

- Seedling SHG (I): this process yields a nanowatt-level SHG signal due to a small intrinsic $\chi^{(2)}$ nonlinearity, for example, from surface symmetry breaking²⁰.

¹Microsystems and Nanotechnology Division, Physical Measurement Laboratory, National Institute of Standards and Technology, Gaithersburg, MD, USA.

²Institute for Research in Electronics and Applied Physics and Maryland NanoCenter, University of Maryland, College Park, MD, USA. ³Joint Quantum Institute, NIST/University of Maryland, College Park, MD, USA. ⁴Department of Chemistry and Biochemistry, University of Maryland, College Park, MD, USA. ✉e-mail: xiyuan.lu@nist.gov; kartik.srinivasan@nist.gov

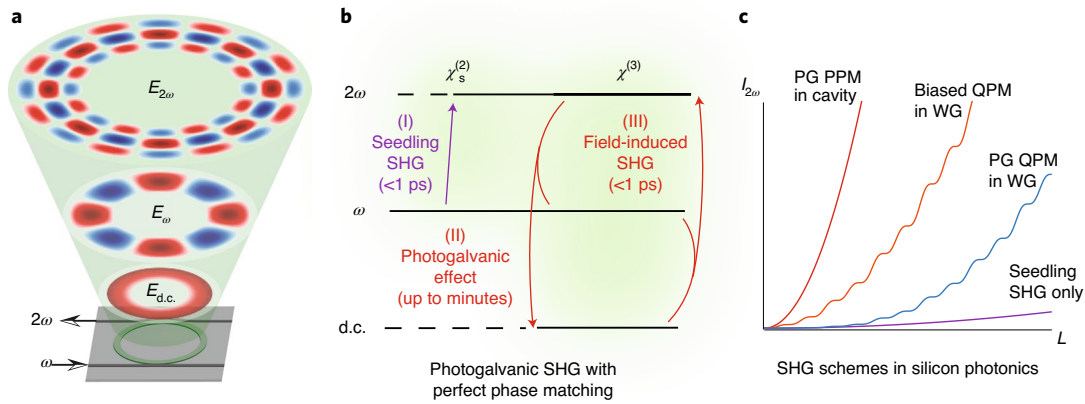


Fig. 1 | Photoinduced SHG in a Si_3N_4 microring resonator. **a**, Illustration of the device and modes involved in perfect phase matching. A Si_3N_4 microring is integrated with two coupling waveguides for pump (ω) and SHG (2ω) light. Within the microring, the mode profiles of three interacting modes at 2ω , ω and d.c. frequencies are shown from top to bottom. Red and blue indicate positive and negative phases of the electric fields, that is, pointing outwards or inwards in the radial direction. The darkness of the colours depicts the local field strength. These modes satisfy perfect phase matching for both $\chi^{(2)}$ and $\chi^{(3)}$ processes. We note that, while the azimuthal distribution of the d.c. field is uniform (due to the perfect phase matching), the exact radial distribution pattern of the d.c. field is unknown and is assumed to be uniform here as a rough estimate when, for example, extracting the device's effective $\chi^{(2)}$. **b**, Photogalvanic SHG with perfect phase matching in a microring. (I) A small seedling SHG (2ω) field is generated with a weak seedling intrinsic $\chi_s^{(2)}$ nonlinearity. (II) This 2ω field, together with the ω field, builds up a d.c. field through the coherent photogalvanic effect, which is distinctively slow (up to minutes) compared with ordinary nonlinear optical processes (<1 ps). (III) The generated d.c. field and the pump field in turn generate SHG light through a field-induced SHG effect, that is, the d.c. Kerr effect. Once seeded by (I), (II) and (III) work together to build up the SHG field. **c**, Our SHG scheme (red) is superior in power efficiency to other processes in $\chi^{(2)}$ silicon photonics, including biased QPM²¹ (orange), photogalvanic QPM^{23,24,26} (blue) and high-Q resonators with weak nonlinearities^{19,20} (purple). This toy model is used to compare the physics of our scheme to related SHG processes in silicon photonics and is qualitative in nature. It only considers QPM and the threshold of the process, and cavity Q enhancement is not considered for illustration purposes. The cavity will provide an additional enhancement related to its finesse. See the Supplementary Information for more details. PG, photogalvanic; PPM, perfect phase matching; WG, waveguide.

- Photogalvanic effect (II)^{39,40}: this process coherently builds up a d.c. electric field through the pump field and the seedling SHG field. The d.c. field can be very large, up to $1 \times 10^7 \text{ V m}^{-1}$ (ref. ⁴¹).
- Field-induced SHG (III)⁴²: the electric field generated by the photogalvanic effect combines with the medium's $\chi^{(3)}$ to create an effective $\chi^{(2)}$ nonlinearity, which in turn amplifies the SHG field (and hence the photogalvanic effect).

Importantly, the scheme is unique in the context of photoinduced SHG in realizing perfect phase matching for both the intrinsic $\chi^{(2)}$ process and the field-induced $\chi^{(2)}$ process simultaneously. Such perfect phase matching is sometimes referred to as modal phase matching; however, here, we use perfect phase matching specifically to distinguish from cases where engineered modal dispersion and quasi-phase matching are used together^{15,43}. First, phase and frequency matching of the intrinsic $\chi^{(2)}$ process, as shown in Fig. 1b, interaction (I), is supported by recent techniques developed in nanophotonic dispersion engineering³². Once such matching is fulfilled, the $\chi^{(3)}$ processes, as shown in Fig. 1b(II,III), are automatically matched given the nature of the d.c. field, which is stationary, with zero angular momentum and a frequency of $\omega = 0$. The $\chi^{(2)}$ and $\chi^{(3)}$ processes can therefore work together seamlessly; that is, the induced $\chi^{(2)}$ can feed on the intrinsic seedling SHG to self-start (Fig. 1b), rather than relying on external electrodes²¹ or a SHG laser for initiation²³. Second, the field-induced $\chi^{(2)}$ in our scheme, through perfect phase matching with a d.c. field, is more efficient than those reported previously, which are achieved through quasi-phase matching with radio-frequency (RF) fields^{21,23,24,26}, as shown in Fig. 1c. Owing to such perfect phase matching, our induced $\chi^{(2)}$ from the d.c. field is always at its maximum, instead of having periodic modulations that decrease the effective $\chi^{(2)}$ to $2/\pi$ and $1/\pi$ times the maximum value for square²¹ and sinusoidal^{23,24,26} longitudinal profiles of the RF fields, respectively. Moreover, the resonance nature enables

the induced $\chi^{(2)}$ to remain spatially uniform inside the resonator, instead of forming build-up and decay-down regions as observed in waveguide geometries^{23,24,26}. Through this phase-matched, photoinduced and resonant SHG process, we report a SHG conversion efficiency of $(2,500 \pm 100) \% \text{ W}^{-1}$ in a Si_3N_4 microring resonator, which is two to four orders of magnitude larger than previous works in typical silicon-based materials^{19–26,44}. Our absolute SHG efficiency is $(22 \pm 1) \%$ at an output power of $(1.9 \pm 0.1) \text{ mW}$, with an input pump power of $(8.8 \pm 1.0) \text{ mW}$. This performance level is promising for $f-2f$ self-referencing of octave-spanning microresonator frequency combs within a common Si_3N_4 platform^{24,29,30}. Moreover, considering the recent integration of Si_3N_4 photonics with Rb vapour cells^{45,46}, high-performance stabilization of telecom lasers (which have also recently been integrated with Si_3N_4 photonics^{47,48}) through efficient SHG that connects the lasers to narrow-linewidth atomic transitions⁴⁹ may now be possible within a single integrated photonic platform.

The SHG device is a Si_3N_4 microring integrated with two coupling waveguides, as shown in Fig. 1a. A pump laser in the telecom band ($\sim 1,560 \text{ nm}$) is coupled by a straight waveguide (bottom) into the microring, in which the $1,560\text{-nm}$ light is frequency-doubled to 780 nm , and the 780-nm light is coupled out by a separate waveguide (top). This top waveguide only supports the 780-nm light; it does not support any modes for $1,560 \text{ nm}$ (see the Supplementary Information for more details on coupling). Inside the microring, three modes are involved in the process, the d.c. mode, the pump mode ($1,560 \text{ nm}$) and the SHG mode (780 nm). The d.c. mode is stationary (resonance frequency of $\omega = 0$) with zero azimuthal angular momentum, and can be characterized by $(n, m) = (0, 0)$ when depicted in the whispering gallery mode terminology, where n represents the radial mode number and m represents the azimuthal mode number. To perfectly match the mode numbers for the pump and SHG, we use the fundamental transverse-electric

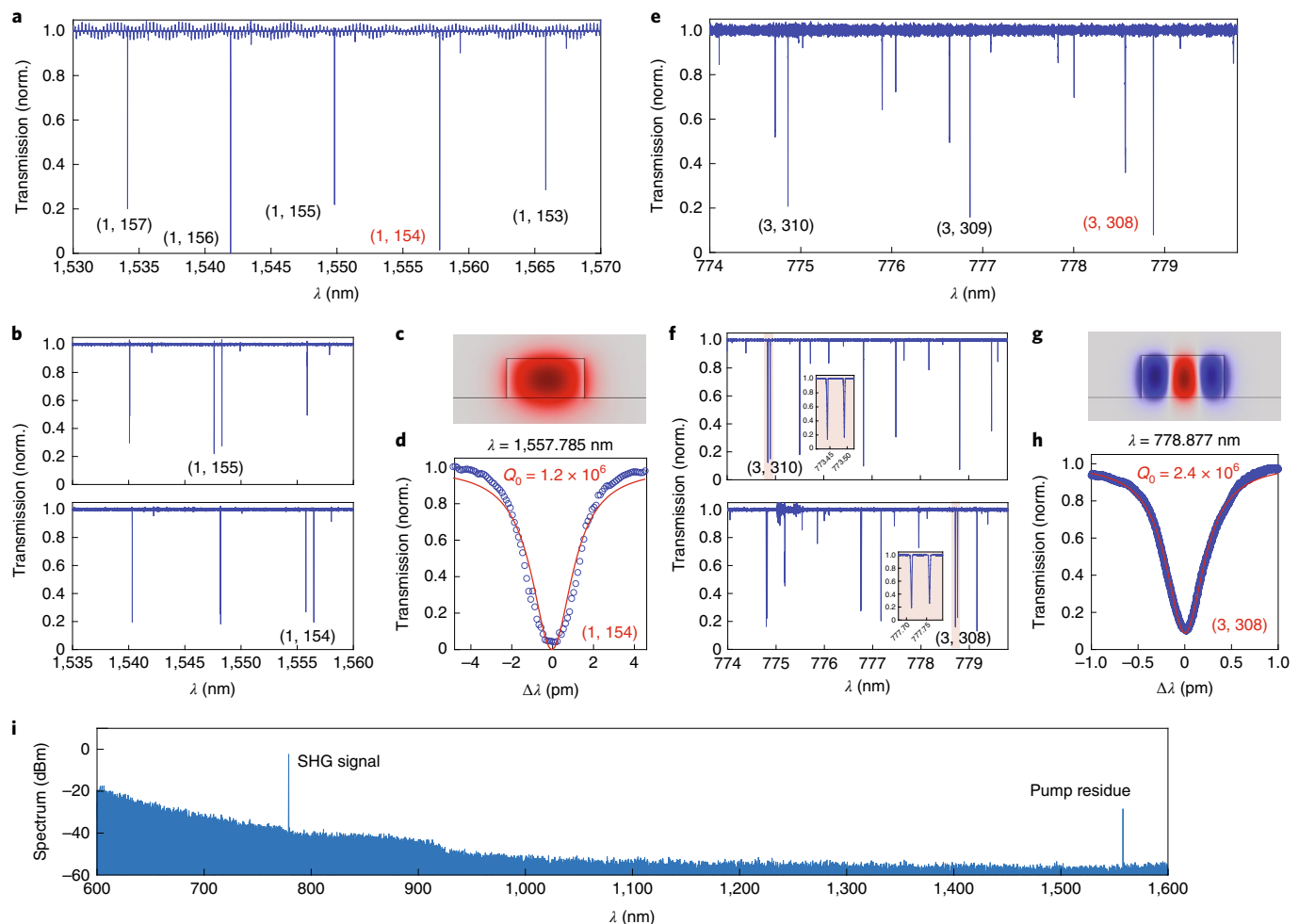


Fig. 2 | Device transmission shows perfect phase matching with high-Q resonances. a–h, Pump (a–d) and SHG (e–h) mode characteristics.

a,e, Normalized cavity transmission (T) in the 1,550-nm band (**a**) and the 780-nm band (**e**). The modes are labelled (n, m) , where n and m represent radial and azimuthal mode numbers. In particular, the $(1, 154)$ and $(3, 308)$ modes (labelled in red) satisfy perfect phase matching and are used in the experiment as pump and SHG modes. **b**, The pump mode number is identified using mode-splitting devices targeting $(1, 155)$ and $(1, 154)$, respectively, and the corresponding cavity modes are clearly identified by a mode splitting of ~ 0.7 nm. **f**, For 780-nm band modes, that is, the $(3, 310)$ and $(3, 308)$ modes, the mode splittings are ~ 45 pm, as shown in the insets. **c,g**, Cross-sectional field profiles for the pump and SHG modes. **d,h**, The pump and SHG modes, that is, $(1, 154)$ and $(3, 308)$, have wavelengths of 1,557.785 nm and 778.877 nm at 21.9 °C in the cold cavity (without Kerr shift or thermal bistability). Their intrinsic Q values are $(1.2 \pm 0.1) \times 10^6$ and $(2.4 \pm 0.1) \times 10^6$, and the loaded Q values are $(6.0 \pm 0.5) \times 10^5$ and $(1.6 \pm 0.1) \times 10^6$, respectively. The errors represent 1 s.d. uncertainties in nonlinear fitting of the resonances. **i**, The measured SHG response (from the 2ω waveguide depicted in Fig. 1a) once the fundamental and second-harmonic modes are frequency-matched has a clean spectrum without conversion into untargeted modes. The background increase at shorter wavelengths is from the noise floor of the optical spectrum analyser.

(TE₁) mode for the pump and the third-order transverse-electric (TE₃) mode for the second harmonic, with the respective mode profiles in Fig. 2c,g. Finite-element-method simulation indicates that the $(1, 154)$ and $(3, 308)$ modes, which are clearly matched in angular momentum, have nearly matched frequencies in a microring with 23- μ m radius, 1.2- μ m ring width and 600-nm thickness (additional details regarding dispersion engineering are provided in the Supplementary Information).

To guarantee perfect phase matching of the underlying intrinsic $\chi^{(2)}$ process, we identify the azimuthal mode numbers using the selective mode splitting method⁵⁰ that has recently been applied to wide-band microcavity nonlinear optics³². Using this method, we pattern some devices with small modulations in ring widths (an amplitude of 20 nm) and angular periods of π/m to deterministically scatter and split the m th mode, while leaving other modes unperturbed, as illustrated in Fig. 2b,f. For example, spectra from two devices exhibiting a targeted mode splitting at $\sim 1,548$ nm

($m = 155$) and $\sim 1,557$ nm ($m = 154$) are shown in Fig. 2b. We also use this method to identify the 780-nm modes, as shown in Fig. 2f. Devices on the same chip with the same nominal dimensions, but without the mode-splitting pattern, show very similar resonance wavelengths (Fig. 2a,e), so relative modes for all devices on the chip can be identified. The tight constraint associated with perfect phase matching using high-Q whispering gallery mode resonances results in a spectrally clean SHG response once the fundamental and second harmonic modes are frequency-matched, without unwanted conversion into modes other than the targeted one, as shown in Fig. 2i.

Although phase matching is quantized and is perfect once the appropriate modes are identified, frequency matching of those modes typically needs thermal/power tuning⁶, as shown in Fig. 3a,b. The device has loaded quality factors of $>0.5 \times 10^6$ and intrinsic Q values of $>1 \times 10^6$ for both pump and SHG modes (Fig. 2d,h). These high Q values necessitate frequency matching to be within ~ 0.3 GHz

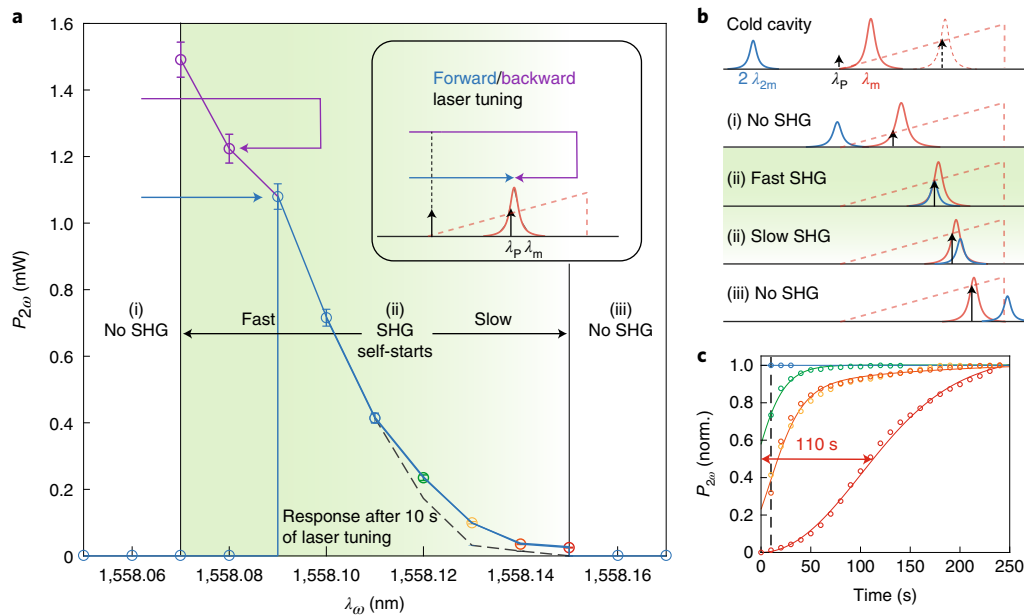


Fig. 3 | Laser detuning to optimize photoinduced SHG in the microring. **a, b**, Experimental results (**a**) and illustrations (**b**) showing three regions with a distinct SHG response. In **b**, the x axis represents the wavelength and SHG can happen when the pump mode wavelength (λ_p) and twice the SHG mode wavelength ($2\lambda_m$) overlap (this is equivalent to the overlap of ν_{2m} and $2\nu_m$, but the schematic is drawn from the experimental perspective in which light is injected into the telecom mode as the wavelength is increased, as in **a**). In regions (i) and (iii), the device has no observed SHG response, because of the inefficient seedling SHG process, as the cavity modes are frequency-mismatched. In region (ii) (green area), the cavity frequencies match and photoinduced SHG can self-start, either through forward (blue) or backward (purple) laser tuning. As shown in the inset, both tuning methods require forward tuning at first to drop laser power into the cavity, because of thermal bistability indicated by the dashed red line, whose height is proportional to the pump power that is dropped into the cavity. In region (ii), photoinduced SHG can self-start and the response time depends on the laser detuning, which affects the cavity frequency mismatch, as shown in **b(ii)**. Darker green indicates a faster response in region (ii). The dashed black line in **a** indicates the output SHG power after the laser is tuned for 10 s. The error bars in **a** represent 1 s.d. uncertainties from the calibration of the on-chip power. **c**, The response takes a few seconds or less than a second when the pump is below 1,558.11 nm (blue), and takes from 20 s at 1,558.12 nm (green) to 110 s at 1,558.15 nm (red). This slow response is a signature of the photogalvanic process, in contrast to other nonlinear processes that are typically ultrafast (<1 ps). The dashed black line indicates a time of 10 s after laser tuning, corresponding to that in **a**. The lines are guides to the eye.

(the cavity linewidth). The resonance wavelengths of the pump and SHG modes are 1,557.785 nm and 778.877 nm, respectively, recorded by a wavemeter at room temperature when the optical power is small so that both Kerr and thermo-optic shifts are negligible. The SHG mode thus needs an ~ 7.7 -GHz (15.5 pm) redshift relative to that of the pump mode to enable frequency matching, as illustrated in the top panel of Fig. 3b. Such a frequency mismatch can be compensated by both thermal and Kerr effects. In particular, the thermal shift can make up for this frequency mismatch by heating at a rate of 0.291 GHz per $^{\circ}\text{C}$ (0.585 pm per $^{\circ}\text{C}$) (details are provided in the Supplementary Information).

The thermo-optic bistability exhibited by the high-Q cavity, indicated by dashed red triangles in Fig. 3a,b, requires the pump laser to be scanned from blue detuning to red detuning to drop power into the cavity. When pump power is first dropped into the cavity, illustrated by region (i) in Fig. 3a,b, the pump and SHG mode are mismatched in frequency, similar to the cold cavity case. Here, the seedling SHG process is only resonantly enhanced by the pump cavity mode but not by the SHG cavity mode, and yields no observable SHG signal (the minimum power our detector can resolve is 0.1 nW). Without such seedling SHG, effective photoinduced SHG cannot self-start. When the pump laser is tuned into region (ii) in Fig. 3a,b, the two cavity modes start to have spectral overlap, which results in an appreciable seedling SHG power to start the photogalvanic effect.

To reach optimal SHG power, both forward and backward tuning of the pump laser are required, with the specifics dependent on the laser-cavity detuning. These two tuning methods are illustrated in the inset of Fig. 3a. For example, the SHG power of 1.15 mW can

be directly generated by forward tuning, where the laser is tuned from $<1,558.06$ nm to 1,558.09 nm, as indicated by the blue arrow. However, the larger SHG power of ~ 1.2 mW at 1,558.08 nm can only be accessed through backward tuning; that is, the laser is first tuned in the forward direction from $<1,558.06$ nm to $>1,558.09$ nm, and then tuned in the backward direction to 1,558.08 nm, as indicated by the purple arrow. In comparison, when the laser is directly forward-tuned from $<1,558.06$ nm to 1,558.08 nm, no SHG signal is observed. Such hysteresis is probably due to pump depletion, as the cavity frequency matching is different when SHG just starts (without depletion) in comparison to when it has already started (with depletion). We have verified that with a lower input power (~ 4 mW), such hysteresis is substantially decreased.

As discussed earlier, when the pump laser is set to a wavelength between 1,558.09 nm and 1,558.15 nm, SHG can self-start simply by forward tuning. The response time of the process is determined by the photogalvanic process. This time depends critically on the cavity frequency matching. When the frequency is matched well (top panel (ii), Fig. 3b), that is, $\lambda_p = 1,558.09$ –1,558.11 nm, the response time is within a few seconds. By contrast, when the cavity modes are not well frequency-matched (bottom panel (ii), Fig. 3b), that is, $\lambda_p = 1,558.12$ –1,558.15 nm, the SHG has a slow build-up time ranging from 20 s to over a minute, as shown in Fig. 3c. Note that our photogalvanic build-up time is much shorter than those reported in previous works. Even the slowest case has a response of ~ 110 s, and this response time is in general two to three orders of magnitude faster than previous photogalvanic work in waveguides^{23,24,26}. Such a notable change in response time is related to the cavity enhancement

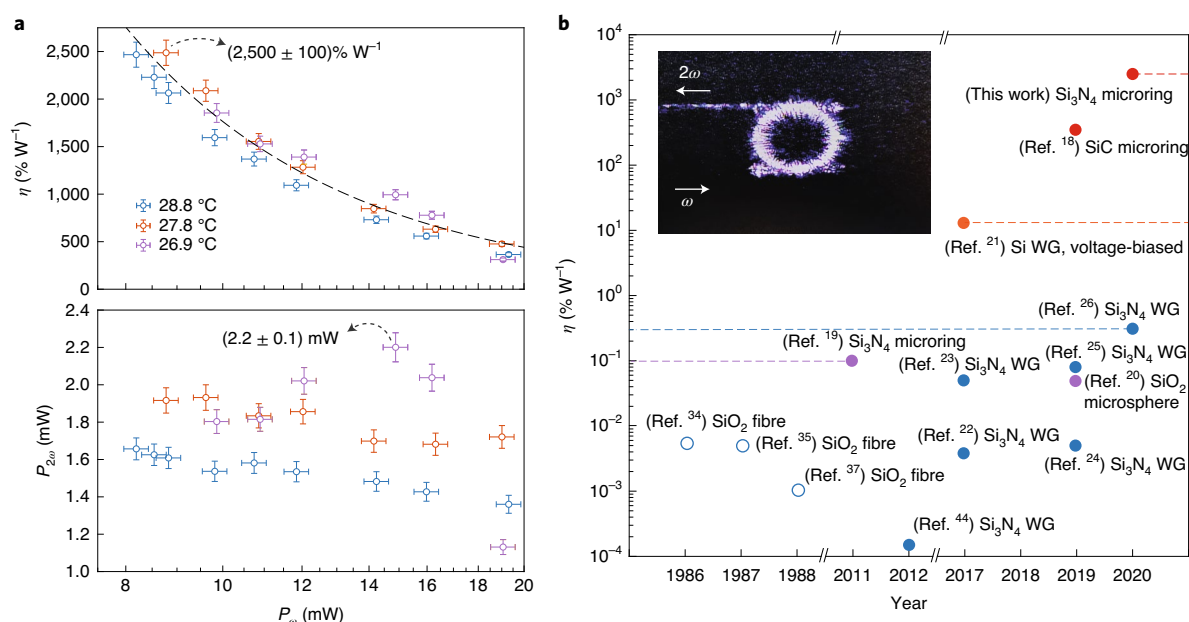


Fig. 4 | High efficiency is achieved by photoinduced SHG in silicon photonics. **a**, An efficiency of $(2,500 \pm 100)\% \text{ W}^{-1}$ is obtained with the laser detuning and thermal tuning (top). The normalized efficiency is given by $\eta = P_{2\omega}/P_{\omega}^2$, where P_{ω} and $P_{2\omega}$ represent the pump and SHG powers in the waveguides on chip, respectively. The SHG power is $(2.2 \pm 0.1) \text{ mW}$ when pumped with 15 mW at 26.9°C (bottom). The error bars represent 1 s.d. uncertainties from the calibration of the on-chip power. The dashed line is a guide to the eye. **b**, A comparison with other SHG works in silicon photonics shows that our SHG efficiency is high. Inset: the generation of SHG light by a telecom pump. The complementary metal-oxide-semiconductor (CMOS) camera is responsive to 780-nm light but not telecom light. The image clearly shows the generation of SHG light in the microring and the coupling of light into the top waveguide, as indicated by the arrow. WG, waveguide. The dashed lines are guides to the eye.

in the SHG efficiency. Although in the waveguides the SHG signal has to build up longitudinally, the SHG signal can pass through the cavity $\sim 5,000$ times to build up coherently. This number of roundtrips of light is estimated by $\mathcal{F}/(2\pi)$, where \mathcal{F} is the cavity finesse. Finally, when the laser is further detuned into region (iii) in Fig. 3a,b, the cavity frequency mismatch is over-compensated, so that the SHG mode is redshifted relative to the pump mode.

We repeated this method at various pump powers and temperatures to optimize the normalized conversion efficiency (η) and output power ($P_{2\omega}$), as shown in Fig. 4a. The top panel shows that the maximal normalized conversion efficiency ($\eta = P_{2\omega}/P_{\omega}^2$) is $(2,500 \pm 100)\% \text{ W}^{-1}$. The maximal value is realized by optimizing the pump power, cavity detuning and device temperature. This value is related to several factors, including frequency matching, changing nonlinearity and pump depletion, which are difficult to disentangle. At the lower power end, efficient SHG is not achieved, and such an abrupt change depends on temperature (a higher temperature allows a smaller pump power to have efficient photoinduced SHG). We note that the reason we use the $\% \text{ W}^{-1}$ figure of merit is because it is commonly cited in the silicon photonics community and we want to provide a point of comparison to the earlier works.

By comparison, as shown in Fig. 4b, this efficiency (dashed red line) is >100 times the previously reported result of $13\% \text{ W}^{-1}$ in silicon photonics²¹ (dashed orange line). Our results have superior efficiency compared to previous works due to the use of perfect phase matching and resonant enhancement rather than quasi-phase matching in waveguides^{21–26,44} (dashed blue line) and silica fibres^{34–37}, while our much larger nonlinearity leads to improved performance relative to all other resonant schemes in silicon photonics^{19,20} (dashed purple line). We note that the efficiency does not show a linear dependence on pump power, because, unlike an intrinsic $\chi^{(2)}$ or a $\chi_{\text{eff}}^{(2)}$ enabled by a constant electric field (for example, via electrodes), the $\chi_{\text{eff}}^{(2)}$ here is optically induced and its value depends on the generated SHG signal.

Although our normalized SHG efficiency of $(2,500 \pm 100)\% \text{ W}^{-1}$ is only 1% of the recently reported $\chi^{(2)}$ record in lithium niobate microrings¹⁵, our absolute SHG efficiency of $(22 \pm 1)\%$ (Supplementary Information) is comparable to state-of-the-art $\chi^{(2)}$ nanophotonic devices^{7,15}. Moreover, the maximal SHG power we obtained is $\sim 2.2\text{-mW}$ SHG in the waveguide with $\sim 15\text{-mW}$ input pump power (bottom panel, Fig. 4a). Achieving such milliwatt-level output SHG powers with high conversion efficiency is indicative of how this work demonstrates photoinduced SHG that is comparable to state-of-the-art $\chi^{(2)}$ results^{7,14,15}. The Supplementary Information presents a more detailed discussion of this comparison, as well as the estimated induced $\chi^{(2)}$, d.c. field and related discussions.

The maximal induced $\chi^{(2)}$ value is $\chi^{(2)} = (0.20 \pm 0.04) \text{ pm V}^{-1}$ (Supplementary Information), near the lower end of previous Si_3N_4 photogalvanic results^{22–26}, which range from 0.3 pm V^{-1} to 3.7 pm V^{-1} . The electric field is estimated to be $(0.6 \pm 0.1) \text{ MV cm}^{-1}$, which is $\sim 15\text{--}20\%$ of the electric breakdown voltage of Si_3N_4 (ref. 51), that is, $3\text{--}4 \text{ MV cm}^{-1}$. Our induced nonlinearity is currently limited by pump depletion and can probably be improved further. For example, in previous work²¹, the applied field is 0.25 MV cm^{-1} , which is 62.5% of the electric breakdown voltage of Si (0.40 MV cm^{-1}). Operation near the breakdown field of silicon nitride, for example, 4 MV cm^{-1} , suggests an upper-bound estimate of 1.3 pm V^{-1} as potentially accessible in our system.

Efficient SHG only occurs in our system at sufficiently high (milliwatt-level) injected powers, and an unsolved problem for photogalvanic SHG is the origin and value of such threshold powers. Previously, such threshold behaviour has only been reported empirically in fibre (5-kW peak power)³⁵ and waveguide (10-W peak power)²², both using quasi-phase matching and pulse pumping. We believe our system, with perfect phase matching and continuous-wave pumping at milliwatt levels, is a promising platform to probe the origin of this threshold, for example, whether it

comes from the photogalvanic process alone or the overall nonlinear process.

In summary, we have demonstrated efficient photoinduced SHG with perfect phase matching in silicon photonics, achieving record-high conversion efficiencies in comparison to prior silicon-based devices, and absolute efficiencies and output powers on par with the highest values demonstrated in nanophotonic media with much larger intrinsic $\chi^{(2)}$ nonlinearities. Our demonstration opens up promising avenues for $\chi^{(2)}$ nonlinear silicon photonics, including f – $2f$ locking for $\chi^{(3)}$ -mediated octave-span frequency combs, SHG-based connections between telecom lasers and atom-based frequency standards, sum/difference-frequency generation and electro-optical modulation. Going forward, the integration of external electrodes to create the d.c. electric field can enable efficient SHG across a wider range of input powers, produce a larger effective $\chi^{(2)}$ response and realize additional levels of tunability and control.

Online content

Any methods, additional references, Nature Research reporting summaries, source data, extended data, supplementary information, acknowledgements, peer review information; details of author contributions and competing interests; and statements of data and code availability are available at <https://doi.org/10.1038/s41566-020-00708-4>.

Received: 14 February 2020; Accepted: 24 September 2020;

Published online: 2 November 2020

References

- Boyd, R. W. *Nonlinear Optics* (Academic Press, 2008).
- Spencer, D. T. et al. An optical-frequency synthesizer using integrated photonics. *Nature* **557**, 81–85 (2018).
- Singh, N. et al. Silicon photonics optical frequency synthesizer—SPOFS. In *2019 Conference on Lasers and Electro-Optics/ATh41.2* (IEEE, 2019).
- Newman, Z. L. et al. Architecture for the photonic integration of an optical atomic clock. *Optica* **6**, 680–685 (2019).
- Xue, X. et al. Second-harmonic-assisted four-wave mixing in chip-based microresonator frequency comb generation. *Light Sci. Appl.* **6**, e16253 (2017).
- Guo, X., Zou, C.-L. & Tang, H. X. Second-harmonic generation in aluminum nitride microrings with 2,500%/W conversion efficiency. *Optica* **3**, 1126–1131 (2016).
- Bruch, A. W. et al. 17,000%/W second-harmonic conversion efficiency in single-crystalline aluminum nitride microresonators. *Appl. Phys. Lett.* **113**, 131102 (2018).
- Bruch, A. W., Liu, X., Surya, J. B., Zou, C.-L. & Tang, H. X. On-chip $\chi^{(2)}$ microring optical parametric oscillator. *Optica* **6**, 1361–1366 (2019).
- Bruch, A. W. et al. Pockels soliton microcomb. *Nat. Photon.* <https://doi.org/10.1038/s41566-020-00704-8> (2020).
- Chang, L. et al. High efficiency SHG in heterogenous integrated GaAs ring resonators. *APL Photon.* **4**, 036103 (2019).
- Chang, L. et al. Thin film wavelength converters for photonic integrated circuits. *Optica* **3**, 531–535 (2016).
- Wang, C. et al. Ultrahigh-efficiency wavelength conversion in nanophotonic periodically poled lithium niobate waveguides. *Optica* **5**, 1438–1441 (2018).
- Luo, R., He, Y., Liang, H., Li, M. & Lin, Q. Highly tunable efficient second-harmonic generation in a lithium niobate nanophotonic waveguide. *Optica* **4**, 1251–1258 (2018).
- Chen, J.-Y. et al. Ultra-efficient frequency conversion in quasi-phase-matched lithium niobate microrings. *Optica* **6**, 1244–1245 (2019).
- Lu, J. et al. Periodically poled thin-film lithium niobate microring resonators with a second-harmonic generation efficiency of 250,000%/W. *Optica* **6**, 1455–1460 (2019).
- Chang, L. et al. Heterogeneous integration of lithium niobate and silicon nitride waveguides for wafer-scale photonic integrated circuits on silicon. *Opt. Lett.* **42**, 803–806 (2017).
- Song, B.-S. et al. Ultrahigh-Q photonic crystal nanocavities based on 4H silicon carbide. *Optica* **6**, 991–995 (2019).
- Lukin, D. M. et al. 4H-silicon-carbide-on-insulator for integrated quantum and nonlinear photonics. *Nat. Photon.* **14**, 330–334 (2020).
- Levy, J. S., Foster, M. A., Gaeta, A. L. & Lipson, M. Harmonic generation in silicon nitride ring resonators. *Opt. Express* **19**, 11415–11421 (2011).
- Zhang, X. et al. Symmetry-breaking-induced nonlinear optics at a microcavity surface. *Nat. Photon.* **13**, 21–24 (2019).
- Timurdogan, E., Poulton, C. V., Byrd, M. J. & Watts, M. R. Electric field-induced second-order nonlinear optical effects in silicon waveguides. *Nat. Photon.* **11**, 200–206 (2017).
- Porcel, M. A. et al. Photo-induced second-order nonlinearity in stoichiometric silicon nitride waveguides. *Opt. Express* **25**, 33143–33159 (2017).
- Billat, A. et al. Large second harmonic generation enhancement in Si_3N_4 waveguides by all-optically induced quasi-phase-matching. *Nat. Commun.* **8**, 1016 (2017).
- Hickstein, D. D. et al. Self-organized nonlinear gratings for ultrafast nanophotonics. *Nat. Photon.* **13**, 494–499 (2019).
- Grassani, D., Pfeiffer, M. H. P., Kippenberg, T. J. & Brès, C.-S. Second- and third-order nonlinear wavelength conversion in an all-optically poled Si_3N_4 waveguide. *Opt. Lett.* **44**, 106–109 (2019).
- Nitiss, E. et al. Formation rules and dynamics of photoinduced $\chi^{(2)}$ gratings in silicon nitride waveguides. *ACS Photon.* **7**, 147–153 (2020).
- Moss, D. J., Morandotti, R., Gaeta, A. L. & Lipson, M. New CMOS-compatible platforms based on silicon nitride and hydex for nonlinear optics. *Nat. Photon.* **7**, 597–607 (2013).
- Okawachi, Y. et al. Octave-spanning frequency comb generation in a silicon nitride chip. *Opt. Lett.* **36**, 3398–3400 (2011).
- Li, Q. et al. Stably accessing octave-spanning microresonator frequency combs in the soliton regime. *Optica* **4**, 193–203 (2017).
- Karpov, M., Pfeiffer, M. H., Liu, J., Lukashchuk, A. & Kippenberg, T. J. Photonic chip-based soliton frequency combs covering the biological imaging window. *Nat. Commun.* **9**, 1146 (2018).
- Li, Q., Davanço, M. & Srinivasan, K. Efficient and low-noise single-photon-level frequency conversion interfaces using silicon nanophotonics. *Nat. Photon.* **10**, 406–414 (2016).
- Lu, X. et al. Efficient telecom-to-visible spectral translation using silicon nanophotonics. *Nat. Photon.* **13**, 593–601 (2019).
- Lu, X. et al. Milliwatt-threshold visible-telecom optical parametric oscillation using silicon nanophotonics. *Optica* **6**, 1535–1541 (2019).
- Österberg, U. & Margulis, W. Dye laser pumped by Nd:YAG laser pulses frequency doubled in a glass optical fiber. *Opt. Lett.* **11**, 516–518 (1986).
- Österberg, U. & Margulis, W. Experimental studies on efficient frequency doubling in glass optical fibers. *Opt. Lett.* **12**, 57–59 (1987).
- Stolen, R. H. & Tom, H. W. K. Self-organized phase-matched harmonic generation in optical fibers. *Opt. Lett.* **12**, 585–587 (1987).
- Tom, H. W. K., Stolen, R. H., Aumiller, G. D. & Pleibel, W. Preparation of long-coherence-length second-harmonic-generating optical fibers by using mode-locked pulses. *Opt. Lett.* **13**, 512–514 (1988).
- Margulis, W., Laurell, F. & Lesche, B. Imaging the nonlinear grating in frequency-doubling fibres. *Nature* **378**, 699–701 (1995).
- Éntin, M. V. Theory of the coherent photovoltaic effect. *Sov. Phys. Semicond.* **23**, 664 (1989).
- Dianov, E. M., Kazanskii, P. G. & Stepanov, D. Y. Problem of the photoinduced second harmonic generation in optical fibers. *Sov. J. Quantum Electron.* **19**, 575–576 (1989).
- Terhune, R. W. & Weinberger, D. A. Second-harmonic generation in fibers. *J. Opt. Soc. Am. B* **4**, 661–674 (1987).
- Terhune, R. W., Maker, P. D. & Savage, C. M. Optical harmonic generation in calcite. *Phys. Rev. Lett.* **8**, 404–406 (1962).
- Ilchenko, V. S., Savchenkov, A. A., Matsko, A. B. & Maleki, L. Nonlinear optics and crystalline whispering gallery mode cavities. *Phys. Rev. Lett.* **92**, 043903 (2004).
- Ning, T. et al. Efficient second-harmonic generation in silicon nitride resonant waveguide gratings. *Opt. Lett.* **37**, 4269–4271 (2012).
- Stern, L., Desiatov, B., Goykhman, I. & Levy, U. Nanoscale light-matter interactions in atomic cladding waveguides. *Nat. Commun.* **4**, 1548 (2013).
- Hummon, M. T. et al. Photonic chip for laser stabilization to an atomic vapor with 10^{-11} instability. *Optica* **5**, 443–449 (2018).
- Boller, K.-J. et al. Hybrid integrated semiconductor lasers with silicon nitride feedback circuits. *Photonics* **7**, 4 (2019).
- Xiang, C. et al. Narrow-linewidth III-V/Si/Si₃N₄ laser using multilayer heterogeneous integration. *Optica* **7**, 20–21 (2020).
- Poulin, M., Latrasse, C., Touahri, D. & Tétu, M. Frequency stability of an optical frequency standard at 192.6 THz based on a two-photon transition of rubidium atoms. *Opt. Commun.* **207**, 233–242 (2002).
- Lu, X., Rogers, S., Jiang, W. C. & Lin, Q. Selective engineering of cavity resonance for frequency matching in optical parametric processes. *Appl. Phys. Lett.* **105**, 151104 (2014).
- Rauthan, C. & Srivastava, J. Electrical breakdown voltage characteristics of buried silicon nitride layers and their correlation to defects in correlation to defects in the nitride layer. *Mater. Lett.* **9**, 252–258 (1990).

Publisher's note Springer Nature remains neutral with regard to jurisdictional claims in published maps and institutional affiliations.

© The Author(s), under exclusive licence to Springer Nature Limited 2020

Data availability

The data that support the plots within this paper and other findings of this study are available from the corresponding authors upon reasonable request.

Acknowledgements

X.L. thanks L. Vivien for helpful discussions. This work is supported by the DARPA DODOS, ACES and NIST-on-a-chip programmes. X.L. and G.M. acknowledge support under the Cooperative Research Agreement between the University of Maryland and NIST-PML, award no. 70NANB10H193.

Author contributions

X.L. led the design, fabrication and measurement of the SHG devices. G.M., A.R. and K.S. provided assistance with design and measurement. D.A.W. provided assistance

with fabrication. All authors participated in the analysis and discussion of results.

X.L. and K.S. wrote the manuscript with assistance from all authors, and K.S. supervised the project.

Competing interests

The authors declare no competing interests.

Additional information

Supplementary information is available for this paper at <https://doi.org/10.1038/s41566-020-00708-4>.

Correspondence and requests for materials should be addressed to X.L. or K.S.

Reprints and permissions information is available at www.nature.com/reprints.